WAVE DIFFRACTION, AMPLIFICATION AND DIFFERENTIAL MOTION NEAR STRONG LATERAL DISCONTINUITIES

By Peter Moczo and Pierre-Yves Bard

ABSTRACT

Macroseismic observations during various historical and recent earthquakes consistently show an increase of damage on narrow stripes located along strong lateral discontinuities, i.e., along contacts between two materials with very different rigidities. This paper presents a series of numerical investigations into this issue. The model consists of a semi-infinite planar, soft layer embedded in a stiffer bedrock, and impinged upon by vertically incident plane *SH* waves. Computations are based on a finite-difference scheme including anelastic attenuation. Two basic phenomena are observed on such simple lateral discontinuities: the well-known 1D (vertical) resonance, and an efficient wave diffraction from the discontinuity towards the softer side. They induce frequency-dependent amplification and a significant differential motion. A parameter study considering various impedance contrast and damping values shows that the amplification is primarily controlled by the impedance contrast, and to a lesser degree by sediment damping. The amplitude exhibits a slight maximum near the discontinuity, but always remains comparable (within 30%) to the 1D value. Differential motion is also controlled by the impedance contrast. It always exhibits a sharp peak in the immediate vicinity of the discontinuity, the level of which does not depend on sediment damping, and reaches significant values even for moderate incident motion. It is concluded that reported observations of increased damage near such geological structures are very likely connected with effects of differential motion on structures.

INTRODUCTION

Numerous, consistent macroseismic observations show a significant increase in damage intensity on "stripes" located along strong lateral discontinuities, i.e. areas where a softer material lies besides a more rigid one (for instance, ancient faults, anomalous contacts, debris zones, etc.). We will not review here such observations, but simply mention several reports.

The earliest concerns the 1868 Hayward, California, earthquake: "The most destructive effects were largely upon "made land" or alluvial formations, and especially along the lines where the "made land" connected with the solid material along the old high water mark" (Prescott, 1982). Similarly, many reports issued after the Provence (France) 1909 earthquake ($M = 6^+$), a synthesis of which may be found in Levret *et al.* (1986) and Payany (1983), mention a marked increase of intensity on the softer side of such anomalous contacts in the villages of Rognes, La Roque d'Anthéron, Venelles, Beaulieu, and Lambesc.

Although not as clear as in the above reports, damage variations within the city of Valdivia during the 22 May 1960 earthquake in Chile are interpreted by Weischet (1963) to be controlled by strong lateral discontinuities in surficial geology. Following the Skopje, Yugoslavia, earthquake of 26 July 1963, Poceski (1969) presents evidences that "the line of heaviest destruction was along the belt which is defined by the sharp change in the thickness of alluvium" (from about 5 m to more than 20 m).

More recently, Siro (1983) and Ivanovic (1986) presented a synthesis on macroseismic observations during the Irpinia, Italy, earthquake of 23 November 1980 and the Montenegro event of 15 April 1979, respectively. Both draw attention to the potential danger of such contact zones, which may be associated with faults, slope deposits or debris, or edges of alluvial valleys. A more detailed description of some specific examples from the villages of Caposele, Castelgrande, Lioni, Rocca San Felice, and Valva may be found in Cavallin *et al.* (1986) and Siro (1983).

Finally, Yuan *et al.* (1992) report similar and consistent observations in the Shidian basin (Yunnan province, China), located about 300 km from the epicenter of the Longlin earthquake ($M_s = 7.1$, 29 May 1976): the intensity jumps from a value of V to a value of VIII (Chinese scale) within a distance less than 200 m of an old fault separating rock and soft lacustrine deposits and then decreases regularly with increasing distance from the fault down to intensity VI, although the surficial geology does not change.

Such repeated observations have not received much attention, since it is well known that damage usually increases as soil rigidity decreases, as expected from simple computations for vertical soil columns. It must be emphasized, however, that simple 1D models cannot explain why the damage in the above mentioned examples is concentrated in stripes along the contact zones; the present paper is intended to focus on this issue.

In some respects, this problem has already been addressed by many authors. The effect of a sharp vertical discontinuity between two joint quarter-spaces has been addressed in several papers, a list of which may be found in Ben-Zion and Aki (1990). All of them, however, consider the wave field radiated by a line *SH* source located at the discontinuity, and they address exclusively the problem of wave fields radiated from heterogeneous fault zones, which is distinct from the surface diffraction phenomenon that we face here. In addition, the velocity and impedance contrast values considered in these investigations are very small (between 0.6 and 1.5 at most) compared with the values encountered at ground surface (largely exceeding 3).

From another point of view, as far as diffraction is concerned, the recent literature is full of papers dealing with the seismic response of 2D geological structures, with a special attention on alluvial valleys (see Sánchez-Sesma, 1987; Aki, 1988; and Faccioli, 1991, for recent reviews), the edges of which may be considered as one particular case of such "anomalous contacts." Although most of those papers focus on the response of the central part of the valley, they usually show that, as described in early papers by Dezfulian and Seed (1969a, b), ground motion on such edges is highly dependent on many different parameters: local slope, velocity contrast, damping, direction of incoming waves, and frequency. Only one of those papers, however, focuses the discussion on the above mentioned macroseismic observations (Yuan *et al.*, 1992) and concludes that the reported asymmetric, irregular intensity distribution cannot be explained simply on the basis of peak or spectral amplitudes computed with 2D models.

Some further work thus remains to be done in order to understand the origin of these intensity observations. Our goal in the present study is simply to start this work on a simple class of models. We consider the simplest geometrical case, as illustrated in Figure 1, for which the anomalous contact between the two zones is vertical, and the incoming wave is a vertically incident plane *SH*
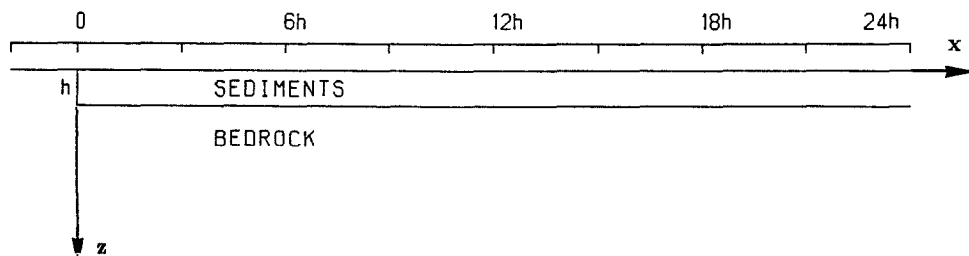
FIG. 1. Model geometry. A semi-infinite layer in a homogeneous half-space. Response has been computed at equidistant sites within the (-1.92 h, 24 h) range along the free surface. $h = 10$ m has been used.

wave. For this model, the relevant parameters are the velocity contrast and damping. Our model is very similar to the one used by Rodriguez et al. (1988), apart from the fact that our bedrock is elastic and not rigid.

After a short description of the finite-difference scheme used in this study (Method section and Appendix A), enlightening models will be presented and their parameters discussed (section on Models). The corresponding results are detailed in the section on Numerical Results, with both the translational motion and the differential (twisting) motion of the surface presented. The final section discusses the connection with the macroseismic observations mentioned earlier in this introduction.

METHOD

Moczo (1989) presented a finite-difference technique using a spatially varying grid spacing for a perfectly elastic medium. Since the "soft" surficial soils we are simulating cannot be accurately considered as nondissipative material, the present study uses a generalization of this technique to absorbing media, based on a method proposed by Emmerich and Korn (1987).

Incorporation of absorption with a realistic frequency dependence into time-domain methods is not an easy task since the stress-strain relation takes the form of a convolution integral. However, when the viscoelastic modulus is approximated by an nth-order rational function of frequency, the viscoelastic stress-strain relation can be transformed into a set of n first-order differential equations. Two ways have been suggested for the determination of the coefficients of these rational function: Day and Minster (1984) used an analytical approach based on the Padé approximation, while Emmerich and Korn (1987) proposed a more efficient and more accurate numerical method. Their approach is based on the rheological model of a generalized Maxwell body (i.e., n classical Maxwell bodies and one spring, all connected in parallel): the rational function then corresponds to the modulus of this generalized Maxwell body, and its coefficients can be interpreted as the relaxation frequencies and weight factors of the classical Maxwell bodies. An optimum is reached when the distribution of the relaxation frequencies follows an equidistant logarithmic scale, over the frequency range of interest. Any desired frequency dependence of the quality factor can be obtained by an appropriate weighting through a numerical curve-fitting process.

Recently, Zahradnik et al. (1990a, b) suggested another approach to incorporate absorption into time-domain methods that provide the complete (not

decomposed into elementary waves) wave field. It consists of an *a posteriori* approximate correction of the solution obtained for a perfectly elastic medium. The approach is computationally more efficient than the method of Emmerich and Korn (1987), but it is restricted to media having a spatially constant quality factor (though an arbitrary power-law frequency dependence may be accounted for). Using the Emmerich and Korn (1987) approach, we are able to account for both an arbitrary damping-frequency law and a spatially varying damping.

The following paragraph gives a brief description of the way the absorption is incorporated into the equations of motion with the finite-difference scheme. A more complete description is given in Appendix A. Further details may be found in Emmerich and Korn (1987) and Moczo (1989).

Equation of Motion

We consider propagation of *SH* waves in a 2-D inhomogeneous medium (x-z plane). Let us denote the density by $\rho(x, z)$, the y component of the displacement vector by $u(x, z, t)$ and the yx and yz components of the stress tensor by σ_{yx} and σ_{yz}, respectively. In the absence of body forces, the displacement u satisfies the homogeneous equation of motion

$$\rho \partial^2 u / \partial t^2 = \partial \sigma_{yx} / \partial x + \partial \sigma_{yz} / \partial z. \tag{1}$$

From Emmerich and Korn (1987), the stress-strain relations are

$$\sigma_{yx} = 2 M_u \cdot \left(0.5 \cdot \partial u / \partial x - \sum_{j=1}^{n} \zeta_{j, yx} \right),$$

$$\sigma_{yz} = 2 M_u \cdot \left(0.5 \cdot \partial u / \partial z - \sum_{j=1}^{n} \zeta_{j, yz} \right), \tag{2}$$

where $M_u(x, z)$ is the elastic, unrelaxed shear modulus, and the functions $\zeta_{j, yx}(x, z, t)$ and $\zeta_{j, yz}(x, z, t)$ satisfy

$$\dot{\zeta}_{j, yx} + \omega_j \zeta_{j, yx} = 0.5 \omega_j Y_j \partial u / \partial x,$$

$$\dot{\zeta}_{j, yz} + \omega_j \zeta_{j, yz} = 0.5 \omega_j Y_j \partial u / \partial z. \tag{3}$$

Here ω_j, $j = 1, 2, \ldots, n$, are the relaxation frequencies, and the coefficients Y_j (related to weight factors) are determined from the K equations:

$$\sum_{j=1}^{n} \frac{\omega_j \cdot \left(\hat{\omega}_k + \omega_j / \hat{Q}(\hat{\omega}_k) \right)}{\omega_j^2 + \hat{\omega}_k^2} \cdot Y_j = 1 / \hat{Q}(\hat{\omega}_k), \qquad k = 1, 2, \ldots, K. \tag{4}$$

The $\hat{\omega}_k$ values correspond to the frequencies at which the quality factor $\hat{Q}(\hat{\omega}_k)$ is specified, so as to obtain the desired frequency dependence. When $K > n$, the system is solved by using a least-square algorithm.

Inserting equations (2) into (1) and using functions $\xi_j(x, z, t)$ defined as

$$\xi_j = 2 \cdot \left(\partial (M_u \zeta_{j, yx}) / \partial x + \partial (M_u \zeta_{j, yz}) / \partial z \right), \tag{5}$$

we obtain

$$\rho \partial^2 u / \partial t^2 = \partial(M_u(\partial u/\partial x))/\partial x + \partial(M_u(\partial u/\partial z))/\partial z - \sum_{j=1}^{n} \xi_j. \quad (6)$$

The only difference between this last equation and that for a perfectly elastic medium comes from the term $\sum_{j=1}^{n} \xi_j$.

Multiplying equations (3) by $2M_u$, differentiating the first and second set of equations with respect to x and z, respectively, and summing them up, we get the final set of n equations:

$$\dot{\xi}_j + \omega_j \xi_j = \omega_j \cdot \left(\partial(P_j(\partial u/\partial x))/\partial x + \partial(P_j(\partial u/\partial z))/\partial z \right), \quad (7)$$

where

$$P_j = M_u \cdot Y_j. \quad (8)$$

This set of equations is solved numerically through the finite-difference algorithm described in Appendix A. It is worth noticing that differences between the definition of ξ_j, equations (6) and (7), and the corresponding ones in the paper by Emmerich and Korn (1987) are due to different approaches in the construction of the finite-difference schemes.

Computational Cost

The memory required in the anelastic case is obviously larger than in the elastic case: the ratio is approximately equal to $(5 + 3n)/5$, n being the number of relaxation frequencies. From numerical tests, Emmerich and Korn (1987) concluded that $n = 3$ provide accurate results for all practical applications. The anelastic calculation then needs an approximately 2.8 times larger memory than the elastic one.

As to the computational time, updating displacement value in one grid point in the anelastic calculation requires $(23 + 14n)/21$ times more arithmetic operations than in the elastic one. When $n = 3$, the CPU time is therefore approximately 3 times larger in the anelastic case.

Test Example

In order to compute the response of arbitrary, heterogeneous 2D geological structures to vertically or obliquely incident plane *SH* waves, a program package called SHFD has been written based on the above formulation. The geologic structure is modeled as a combination of blocks having different parameters. Inside a given block, the velocity, density, and quality factor may vary linearly in the horizontal and vertical directions. The shapes of the interfaces between blocks may be arbitrary; the interface need not coincide with grid points. Both the interface shape and the gradients in the velocity, density, and quality factor are taken into account explicitly in the evaluation of the local effective parameters (equations A1, A2, and A3 in Appendix A). The dependence of the quality factor on frequency may differ from one block to another.

In order to test this formulation, we consider a model derived from the "canonical" sedimentary basin studied first by Boore *et al.* (1971). This basin is sine-shaped, with a half-width of 2500 m, a maximum thickness of 600 m (in its

central part), and a residual thickness of 100 m (on edges). Velocity and density values in the sediments are both linearly increasing with depth: their surface values are, respectively, 0.2 km/sec and 1.6 g/cm^3, while they reach 1.2 km/sec and 2.2 g/cm^3 at a 600-m depth. The velocity and density in the bedrock are spatially constant, and equal to 3.5 km/sec and 3.3 g/cm^3. Further details on geometry, elastic parameters and input motion can be found in Moczo (1989).

We take here a value of 30 for the quality factor inside the basin, and of 1000 in the basement, both at a reference frequency $f_r = 1$ Hz. We follow the recommendations by Emmerich and Korn (1987): three relaxation frequencies ω_j ($n = 3$) are used with the relations $\omega_j/\omega_{j-1} = 10.$, and we take $\omega_3 = 2\omega_{DOM}$, ω_{DOM} being the predominant frequency of the input signal, here $2\pi \cdot 0.25$ Hz. The coefficients Y_j, $j = 1, \ldots, n$ are determined with 5 frequencies $\hat{\omega}_k$, distributed as follows: $\hat{\omega}_1 = \omega_1$, $\hat{\omega}_{k+1} = \hat{\omega}_k \sqrt{\omega_2/\omega_1}$. Causality is maintained through the Futtermann (1962) frequency-dependence relation for Q: $Q(\hat{\omega}_k) = Q_B(\omega_r) - (1/\pi) \cdot \ln(\hat{\omega}_k/\omega_r)$, where $\omega_r = 2\pi f_r$. A comparison between the exact (Futterman's) dependence and the "approximated" (present model) one is shown in Figure 2 for the quality factor in the sediments.

The final results, surface seismograms obtained with the present FD scheme, are compared in Figure 3 with results obtained with Aki-Larner method (Aki and Larner, 1970) as modified by Bard and Bouchon (1985) and Bard and Gariel (1986) to include attenuation and velocity gradient effects. The agreement is very good, though some slight differences may be observed: both techniques (FD and AL) are only approximate methods, and these differences are probably due to numerical errors in both schemes. They are far too small, however, to be significant for practical applications.

MODELS AND GROUND MOTION CHARACTERIZATION

Geometrical and Mechanical Characteristics

In order to investigate the effects of sharp surficial discontinuities, we consider a series of 2D models consisting of a semi-infinite, horizontal, softer layer
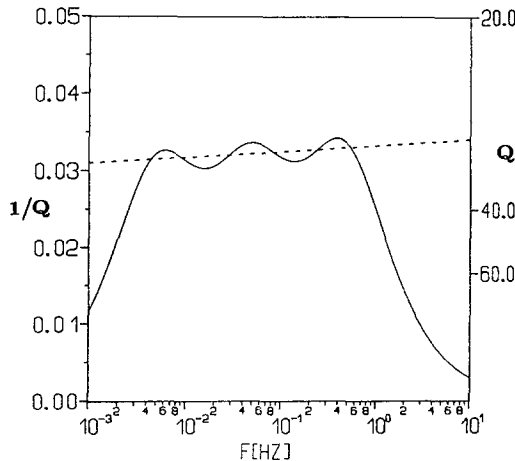
FIG. 2. Comparison between the exact (dotted line) and the approximated (solid line) quality factor ($Q_B = 30$) in the sediments of the test example detailed in the text.
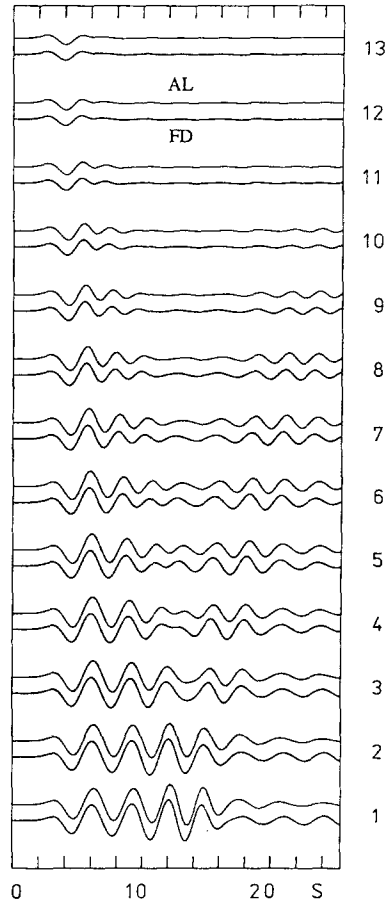
FIG. 3. Comparison between the present finite-difference scheme (FD, lower trace) and the modified Aki-Larner technique (AL, upper trace) for a "canonical" *absorbing* basin. This basin is sine-shaped, with a half-width of 2.5 km, a maximum thickness of 600 m (in its central part), and a residual thickness of 100 m (on edges). Both the velocity and density values in the sediments are linearly increasing with depth: their surface values are, respectively, 0.2 km/sec and 1.6 g/cm^3, while they reach 1.2 km/sec and 2.2 g/cm^3 at a 600-m depth. Their respective, depth-independent counterparts in the bedrock are 3.5 km/sec and 3.3 g/cm^3. The 13 pairs of seismograms correspond to 13 equi-spaced surface sites, from basin center (1, $x = 0$ km) to basin edge (13, $x = 2.4$ km). The incident signal is a Ricker wavelet with a central frequency f_p of 0.25 Hz.

(referred to as "sediments") embedded in a homogeneous, indented, harder "half-space," referred to as "bedrock" (Fig. 1). The contacts between bedrock and sediments are horizontal along a semi-infinite plane giving rise to the classical 1D vertical resonance, and vertical over a thickness h, inducing diffraction effects. The only dimensional parameter of such a model is the layer thickness h, which disappears when the results are expressed as a function of a dimensionless frequency $\eta = f/f_0$, where $f_0 = \beta_s/4h$ is the fundamental frequency of the layer.

Tables 1 and 2 list the material parameters of 12 different configurations that were studied. There are six C (for "constant") models corresponding to homogeneous sediments (i.e., velocity, quality factor, and density values are constant throughout the surficial layer), and another six G (for "gradient") models corresponding to vertically inhomogeneous sediments (i.e., velocity, quality

TABLE 1

MECHANICAL PARAMETERS OF MODELS C*

Model	β_r/β_s	Q_s	β_r (m/sec)	β_s (m/sec)	ρ_s (kg/m^3)	ρ_r (kg/m^3)	Q_r
C-5-50	5	50	1000	200	1800	2200	100
C-5-20	5	20	1000	200	1800	2200	100
C-5-10	5	10	1000	200	1800	2200	100
C-2-50	2	50	400	200	1800	2200	100
C-2-20	2	20	400	200	1800	2200	100
C-2-10	2	10	400	200	1800	2200	100

*Constant velocities, densities, and quality factors.

TABLE 2

MECHANICAL PARAMETERS OF MODELS G*

Model	β_r/β_s (at depth h)	Q_s†	β_s [m/sec]†	ρ_s (kg/m^3)†
G-5-50	4	40 → 60	150 → 250	1750 → 1850
G-5-20	4	16 → 24	150 → 250	1750 → 1850
G-5-10	4	8 → 12	150 → 250	1750 → 1850
G-2-50	1.6	40 → 60	150 → 250	1750 → 1850
G-2-20	1.6	16 → 24	150 → 250	1750 → 1850
G-2-10	1.6	8 → 12	150 → 250	1750 → 1850

*Vertical gradient in velocity, density, and quality factor for the sediments.
† Linearly increasing from free surface to depth h.
β_r, ρ_r, and Q_r are the same as in C models.

factor, and density increase linearly from the surface to depth h). The mean values of velocity, quality factor, and density within the sediments in the G models are equal to the corresponding constant values in C models. The bedrock is homogeneous in all cases.

Both the C and G models include a high (5) and low (2) velocity contrast (β_r/β_s) between sediments and bedrock, and three different levels of attenuation in the sediments: $Q_s(f_r) = 50, 20$, and 10, where the reference frequency f_r is 20 Hz.

Incoming Wave Field

The incoming wave field in this study is a vertically incident plane *SH* wave with time dependency of a Gabor impulse, given by

$$s(t) = e^{-(\omega_p \cdot (t-t_s)/\gamma)^2} \cdot \cos(\omega_p(t - t_s) + \psi),$$

with $t_s = 0.45\gamma/f_p$ and $\omega_p = 2\pi f_p$. We considered two different Gabor signals: (a) in order to obtain Fourier transfer functions in the spectral domain, we used a "δ-like" impulse, referred to in the following as impulse I1, by specifying $f_p = 0.45$ Hz, $\gamma = 0.09$, $\psi = 0$ in the above formula (Fig. 4a); (b) in order to obtain a more monochromatic, though transient, signal, we computed the response of the 12 models to a Gabor signal having the following characteristics: $f_p = 5.0$ Hz, $\gamma = 4.0$, $\psi = \pi/4$ (impulse I2, Fig. 4b).
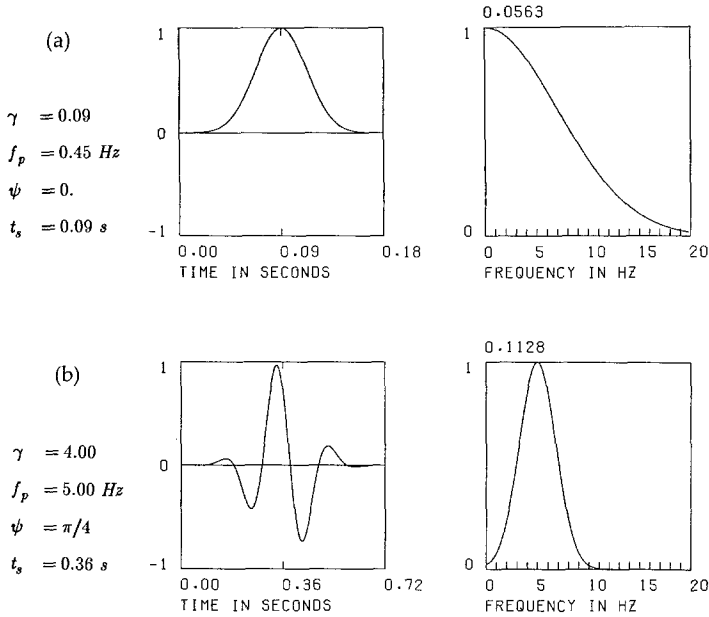
FIG. 4. Frequency and time dependence of the two Gabor signals used in this study. (a) I1 signal; (b) I2 signal. *Left*: time dependence; *Right*: Spectral content (modulus of the Fourier spectrum).

The latter frequency corresponds to the resonance frequency of the 10-m-thick soft layer, which implies a dimensionless frequency value 1.0.

Computations and Characterization of Ground Motion

The "raw" results of our computations are time-domain seismograms at any point of the x-z plane. We consider here only the surface motion, and we compute results according to the following procedure.

First, we first compute the response of each of the 12 models to an I1 Gabor impulse: we use a time step $\Delta t = 0.001$ sec and a total duration T of 2.0 sec for low-contrast models, and $\Delta t = 0.00048$ sec and $T = 3.75$ sec for high-contrast models. This is illustrated in Figure 5a for model C-5-50 at 14 surface sites.

Second, at each surface site, the Fourier transfer function (FTF) is obtained by dividing the Fourier spectrum of the local response to I1 impulse by the Fourier spectrum of the input I1 signal. In all the figures, only the modulus of the FTF is shown (Fig. 5b).

Third, from these FTF, it is easy to compute the time-domain response to an arbitrary input signal. This is done in this study for the I2 Gabor signal (Fig. 5c).

Fourth, as the strong lateral discontinuity has a powerful diffraction effect, we consider not only the translational motion u, but also its spatial derivative $\partial u / \partial x$, in order to estimate the amount of differential motion, in the immediate vicinity of the vertical contact. This differential motion is computed both in the time domain, for I2 input signals (Fig. 5d), and in the frequency domain (i.e., from the spatial derivative of the Fourier transfer functions computed in the second step) (Fig. 5e). The spatial derivative was estimated by simply dividing the difference between the translational motion computed at two adjacent receiver positions by their spacing (i.e., 4.8 m): the values presented from
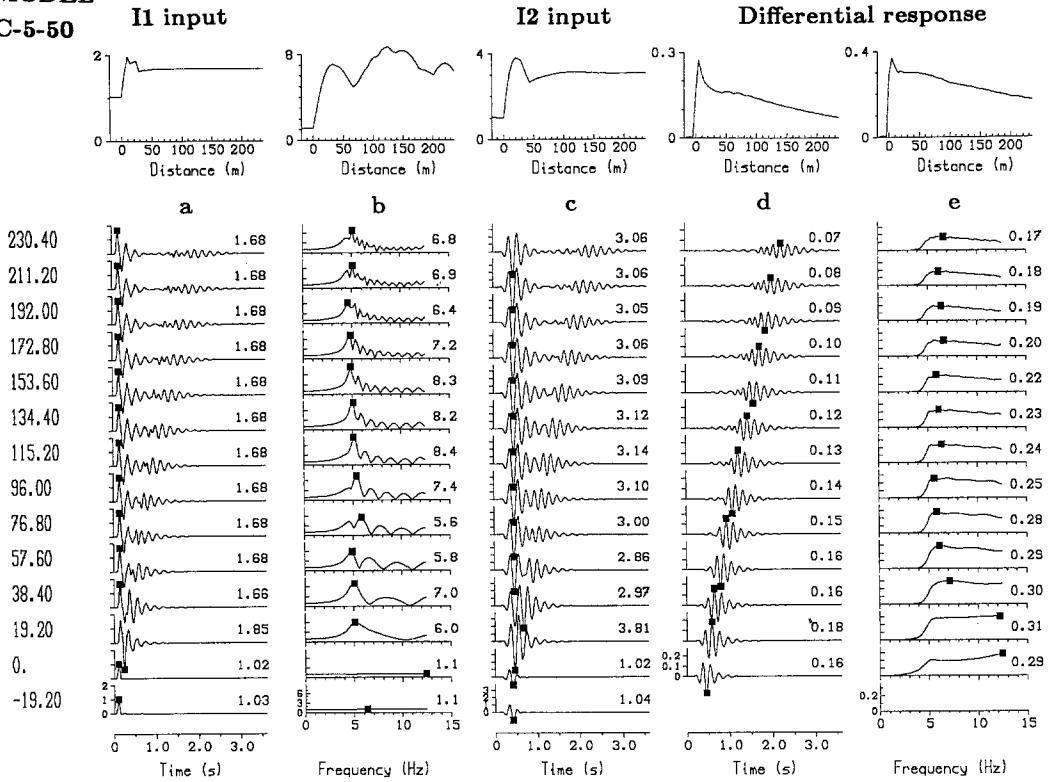
FIG. 5. Results for C-5-50 model: (a) (left column) "Raw" results: response to I1 Gabor pulse (normalized) at 14 equi-spaced surface sites (from $x = -19.2$ m, *bottom*, to $x = 230.4$ m, *top*). (b) Fourier transfer functions at the same surface sites (next column). (c) Response to an I2 Gabor pulse (normalized: amplitude 1 = surface of half-space). (d) Surface differential motion $\partial u / \partial x$ in the time domain for I2 Gabor pulse (= spatial derivative of c). (e) Surface differential motion $\partial u / \partial x$ in the frequency domain (= spatial derivative of b). In each column, numbers to the right represent the peak values of the corresponding quantity for the site under consideration, which is identified through its abscissa x labeled on the left. The five curves on top of each column display the spatial variations of these peak values along a cross-section of the model.

Figures 5 to 11 are then to be considered as only approximate, and lower bounds of the actual differential motion.

All these results may be summarized as displayed in the upper part of Figure 5, where the variations of the corresponding maxima (i.e., I1 impulse time response, Fourier transfer function, I2 time response, I2 differential motion in the time domain, and differential motion in the frequency domain) are plotted as functions of the distance from the discontinuity.

NUMERICAL RESULTS

Diffracted Wave Field

Seismograms in Figure 5a illustrate the wave propagation effects due to such a lateral discontinuity. At sites some distance away from the discontinuity (for instance at $x = 200$ m, i.e., $x = 20$ h), two well-separated wavelets may be clearly identified: the first corresponds to the primary arrival and its subsequent reverberations due to vertical bouncing in the horizontal soft layer, while the second corresponds to waves diffracted away from the discontinuity.

It would be interesting to separate clearly the effects of the horizontal and vertical sections of the interface. However, since the structure is excited by a vertically incident plane wave, it is not possible to investigate the effect of a single vertical contact using a two quarter-spaces model similar to the one investigated by Ben-Zion and Aki (1990). Nevertheless, an interesting insight may be obtained using a model with a relatively large layer thickness (or equivalently, investigating the very-high-frequency response of the model illustrated in Fig. 1). Figure 6 shows the high-frequency response (I1 pulse) of a 120-m-thick semi-infinite layer with the same velocities, densities, and quality factors as in the C-5-50 model. In the computed time window, several well-separated waves in the softer medium may be seen. The first one corresponds simultaneously to the diffracted wave transmitted from bedrock to sediments along the vertical contact with the bedrock velocity, and to the wave diffracted from the upper corner. The second one corresponds mainly to the direct wave transmitted at the deep horizontal interface, and propagating through the layer; however, as shown more clearly on the differential motion seismograms of Figure 6b, this arrival is mixed with, and followed by, weaker phases corresponding to waves diffracted from the lower corner when reached by the incident wave and also by the downgoing wave reflected at the bedrock surface.
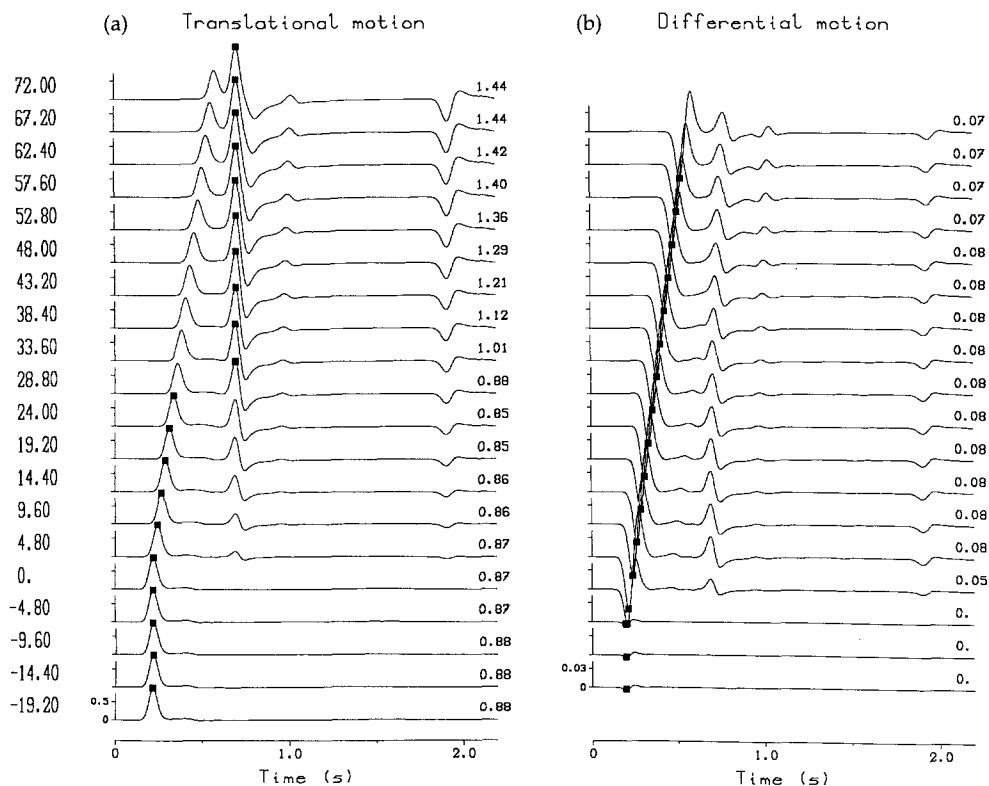
FIG. 6. High-frequency response of a 120-m-thick model. Density, quality factor, and velocity values are the same as for C-5-50 model in Figure 5. (a) Response to I1 Gabor pulse (normalized) at 20 equi-spaced surface sites (from $x = -19.2$ m, *bottom*, to $x = 72.0$ m, *top*). (b) Surface differential motion $\partial u / \partial x$ in the time domain for I1 Gabor pulse (= spatial derivative of a).

These waves are then all bouncing between the free surface and the horizontal sediment-bedrock interface: the late arrival in Figure 6 corresponds to the first of these down-up reflections. It is interesting to notice that, within the sediments, the larger amplitude corresponds to the diffracted wave at very close sites ($x < 0.2\ h$), while at larger distances the direct wave is predominant.

As a consequence, in the immediate vicinity of the discontinuity, the diffracted wave field consists of a combination of oblique body waves, radiated directly from the discontinuity, and multiply reflected at the surface and the bedrock horizontal interface. At large distances, the direct diffracted waves die out because of geometrical spreading and damping, while the multiply reflected waves progressively build up to form a Love wave: the late phase at large distances ($x > 10\ h$) in seismograms of Figures 5a, c, and d corresponds to the phase and group velocities of the first Love modes of the layered half-space.

Effects on Ground Motion

The two dominant effects are classical 1D resonance and lateral diffraction. They result in an abrupt increase of the amplitude of ground motion just across the discontinuity, which is particularly emphasized when the dominant frequency of the incoming signal coincides with the fundamental frequency of the soft layer: for instance, Figure 5c shows that, for a velocity contrast of 5, the amplitude is multiplied by a factor of about 4 over a distance of $2h$ (20 m) in the case of an I2 incident pulse. At larger distance from the discontinuity, the peak (time-domain) amplitude stabilizes around the 1D value corresponding to the local one-layer structure, provided the direct signal is short enough not to overlap the onset of the diffracted surface wave. When this latter condition is not met (i.e., for most real strong motion accelerograms), the peak amplitude may vary in a complicated manner, depending on whether the direct and diffracted waves interfere constructively or destructively.

In addition to the amplification and prolongation of the signal, the presence of a lateral discontinuity results in a significant differential motion (Fig. 5d). For dimensionless frequencies around 1, the differential motion is largest over a very narrow zone (only $2h$ wide) located just to the right of the discontinuity, where it is associated with a complex wave field. Away from the discontinuity, the differential motion is associated with the passage of the Love wave and may be easily estimated with the approximate formula: $\partial u / \partial x \approx 1/c \cdot \partial u / \partial t \approx \omega_p / c \cdot u$, where c is the phase velocity of the Love wave, the lower bound of which is β_s, and ω_p is the dominant frequency of the signal. For the model in Figure 5, the maximum strains (i.e., $0.5 \partial u / \partial x$) reach $1.5 \cdot 10^{-3}$ for a bedrock maximum displacement of 1 cm, which is significant. This value may be compared with the strain predicted by a 1D model for the soft plane layer: in that case, $\partial u / \partial x$ is zero everywhere since there are no laterally propagating waves, while $\partial u / \partial z$ is zero at the (free) surface and maximum at the sediment-bedrock interface, where its order of magnitude is about $5 \cdot 10^{-3}$ for a bedrock maximum displacement of 1 cm. The maximum strain $0.5 \cdot (\partial u / \partial x + \partial u / \partial z)$ experienced by the sediments is therefore not larger in the 2D case. There exists, however, one major difference between 1D and 2D cases: in the latter case, strains reach significant values not only at the sediment-bedrock interface, but also at the surface.

In the frequency domain, the Fourier transfer functions for the soft layer are superpositions of the classical 1D resonance pattern, with bumps around 5 Hz,

and of oscillatory patterns corresponding to the interference between the direct (body) and the diffracted (surface) waves. The frequency spacing of these oscillations shortens with increasing distance from the discontinuity, while their amplitude decreases because of surface wave damping (Fig. 5b). As a consequence, when smoothed Fourier spectral ratios are used instead of "raw" FTF, the differences between 1D and 2D models are hardly visible, except in the immediate vicinity of the discontinuity where the spectral peak is significantly broadened in the latter case.

It is also possible to characterize the differential motion in the frequency domain as shown in Figure 5e. An important result of this figure is that there is no differential motion at frequencies lower than f_0, while it is almost constant (decreasing only very slightly) for frequencies above f_0. It seems therefore rather easy to characterize the spectrum of differential motion, at least for this particular type of models.

Dependence on Mechanical Parameters

Effects of Gradient. Figure 7 shows the results obtained for Model G-5-50 in a similar way as done in Figure 5. The differences between Figures 5 and 7 are small, which is expected since the velocity gradient in model G-5-50 is rather small. Nevertheless, in the presence of a velocity gradient, the effects are larger: the direct waves are more amplified, and the diffracted Love wave, being more
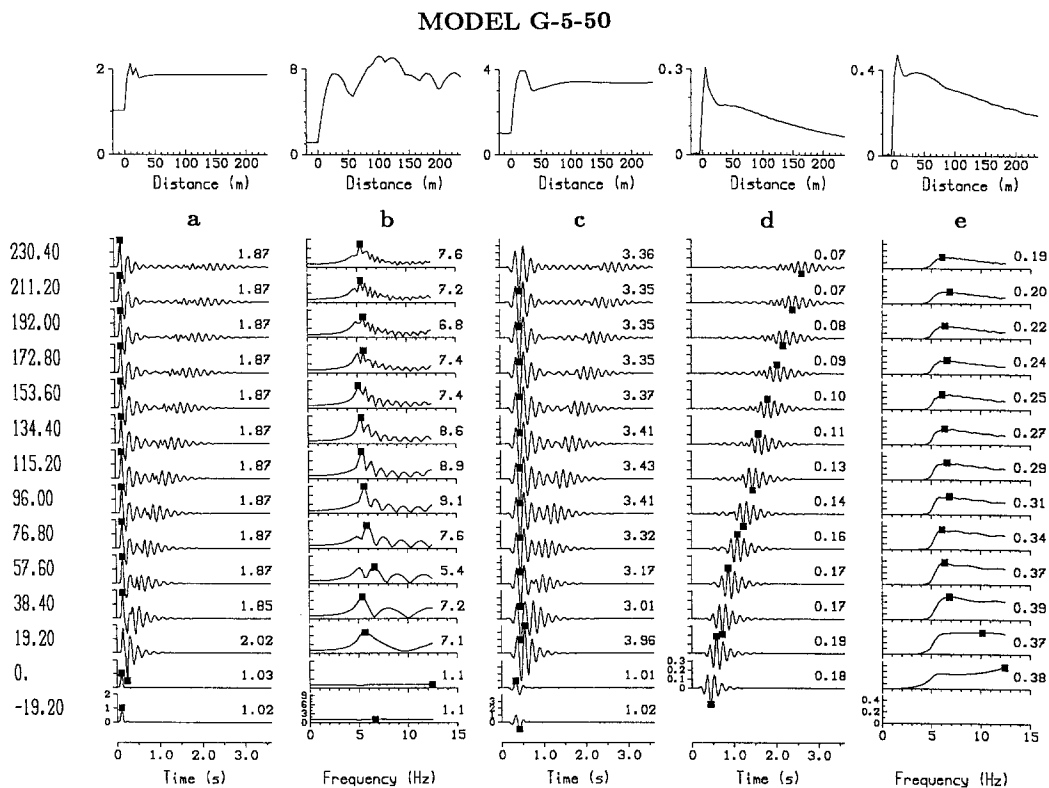
FIG. 7. Similar to Figure 5, but for G-5-50 model.

dispersive, is slower. As a consequence, although the differential motion near the discontinuity is larger for the gradient case, its level is comparable to that of the C model at larger distances (a larger dispersion implies a more efficient damping). In addition, the peak frequencies are slightly shifted towards higher values (by about 15%) in the gradient case, which is consistent with results of simple 1D modelling.

These slight differences are also observed in the case of a lower impedance contrast, as shown in Figure 8. The slight spatial shift observed in the maximum spectral amplification curves of Figure 8a between C and G models corresponds to the fact that the wavelengths are shorter in the latter case.

Effects of Impedance Contrast. Figure 8 shows the (expected) large importance of impedance contrast on the amplification level. Impedance contrast affects both the translational and the differential motion in approximately the same way: when the velocity contrast changes from 5 to 2, the reduction ratio is almost the same for differential and translational motion. This result arises from the fact that the physics of the diffraction phenomena is not altered by the impedance contrast, which affects only their amplitude (see Fig. 9). It is worth noticing, however, that, even in the case of a small contrast, the differential
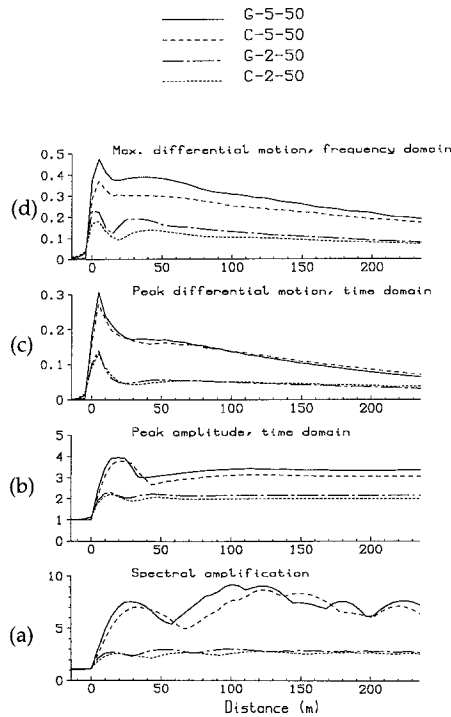
FIG. 8. Summary of effects of impedance contrast and gradient. (a) (*Bottom*) Spatial variation of the peak spectral amplification along a cross section of the model (corresponds to curves on top of Figs. 5b and 7b). (b) (*Second from bottom*) Spatial variation of the peak time-domain amplitude for an incident normalized I2 Gabor pulse (corresponds to curves on top of Figs. 5c and 7c). (c) (*Third from bottom*) Spatial variation of the peak time-domain surface strain for an incident normalized I2 Gabor pulse (corresponds to curves on top of Figs. 5d and 7d). (d) (*Top*) Spatial variation of the peak spectral strain (corresponds to curves on top of Figs. 5e and 7e). Solid, chain-dotted and dotted lines correspond to different models, as displayed on top of the Figure (see Tables 1 and 2).

MODEL C-2-50

FIG. 9. Similar to Figure 5, but for C-2-50 model.

motion reaches significant values: over 10^{-3} for the geometry illustrated in Figure 1 ($h = 10$ m, $\beta_s = 200$ m/sec), and a bedrock maximum displacement of 1 cm (at 5 Hz).

Effects of Damping. In general, the effect of damping is approximately proportional to the ratio between the travel distance and the wavelength. As a consequence, in the present application, it affects much more the diffracted surface wave than the direct arrival, and thus the effects of damping differ depending on the distance from the discontinuity. For instance, comparing Figures 5 and 10, the signals near the discontinuity ($x < 6h$) are only slightly reduced but their shape is not affected, while at larger distances ($x > 15h$), only the direct arrival remains, the amplitude of the surface wave being drastically reduced.

This effect is particularly important for the differential motion, which, at large distances, is related only to the passage of the Love wave. The fall-off of the curves on the top of Figures 10d and 10e is therefore much more rapid than on Figures 5d and 5e. However, their maximum, being near the discontinuity, exhibits the same value independently of the damping considered.

On the other hand, as the direct arrival is an important part of translational motion, the shapes of curves on top of Figures 5a, b, and c are not changed much in Figure 10: they are only shifted downwards, independently of the site position.

MODEL C-5-10

FIG. 10. Similar to Figure 5, but for C-5-10 model.

The effects of damping are summarized in Figure 11 for the four different classes of models (G-5, C-5, G-2, and C-2). The above discussion proves valid for all the considered values of model parameters.

CONCLUSION AND DISCUSSION

Our computations show that strong lateral discontinuities give rise to two basic phenomena: one is the well-known 1D (vertical) resonance and its associated frequency-dependent amplification, and the other an efficient wave diffraction from the discontinuity towards the softer side, which induces an increase in amplification, together with a substantial differential motion.

The amplification is primarily controlled by the impedance contrast, and to a lesser degree by sediment damping. It exhibits a slight maximum near the discontinuity, especially when peak time-domain motion is considered, but it always remains comparable to the 1D value (in the 12 models we investigated, the maximum "overamplification" never exceeds 30%).

Differential motion level is also controlled by the impedance contrast, but its spatial distribution, depending primarily on sediment damping, always exhibits a sharp peak in the immediate vicinity of the discontinuity. In addition, the diffracting efficiency of such lateral discontinuities induces rather high levels of differential motion.

These results are, *stricto sensu*, valid only for the configurations we studied, i.e., step, semi-infinite soft inclusions subjected to vertically incident plane *SH*
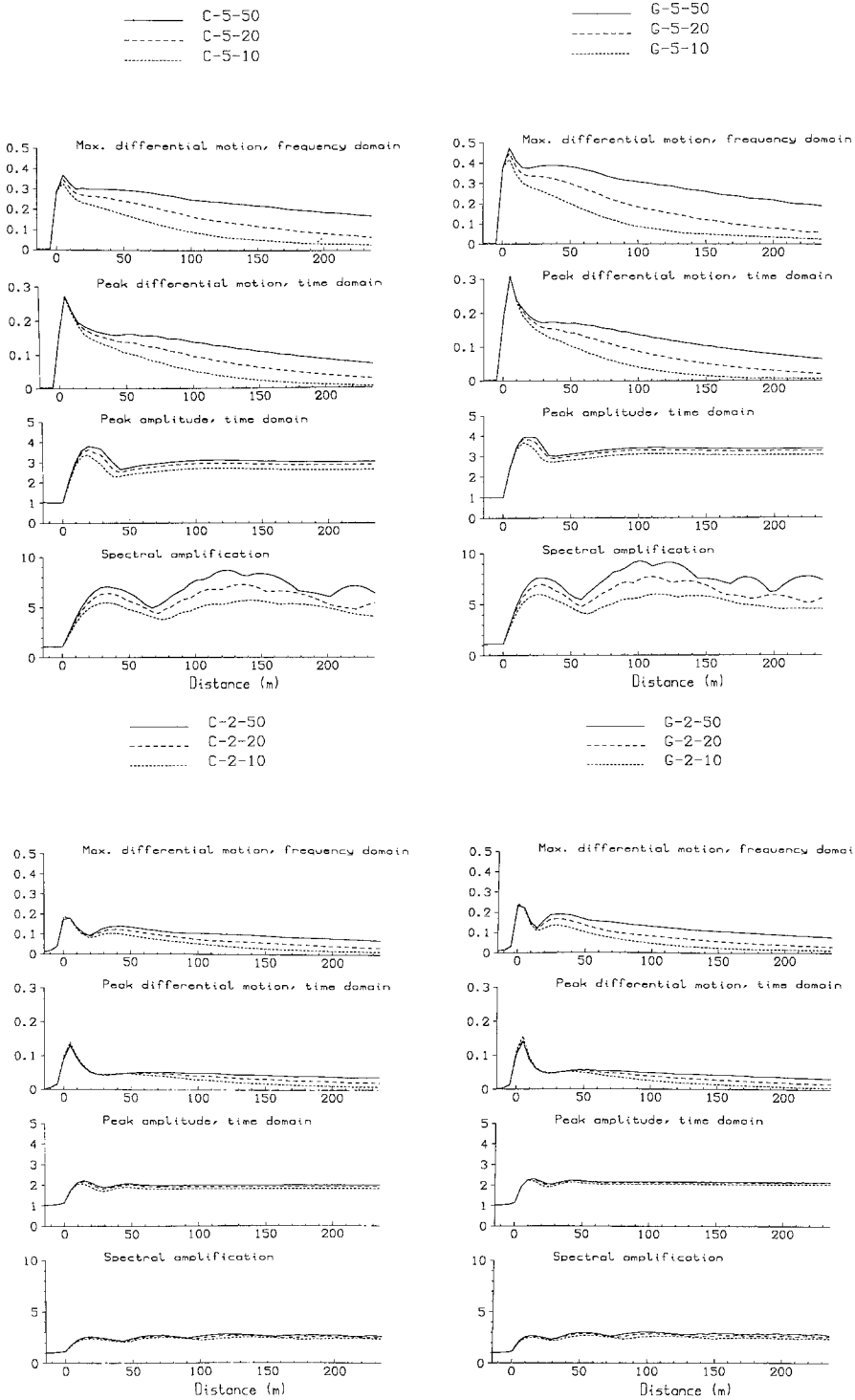
FIG. 11. Summary of effects of damping, for C-5 (*top left*), G-5 (*top right*), C-2 (*bottom left*), and G-2 (*bottom right*) velocity/density structures. The format is identical to format of Figure 8; solid and dotted lines correspond to different Q values (50, 20, and 10).

waves. In case of more realistic impinging wave fields, the lateral discontinuity would give rise to several types of diffracted waves (Rayleigh, grazing *SP*, etc.), and therefore to a more complicated pattern than in the simple *SH* case studied here. However, the results of practical interest for engineering purposes would, in our opinion, remain similar from a qualitative point of view: waves diffracted from the discontinuity will propagate laterally in the soft layer and develop differential motion at ground surface. We thus believe that our present results, though limited, may be used, at least from a qualitative viewpoint, to interpret the damage observations that were mentioned in the introduction.

As already emphasized, 1D models cannot explain the observed concentration of damages in narrow stripes along lateral discontinuities. The main differences between 1D and 2D models are related with the locally diffracted body and surface waves. There are several examples where such locally generated surface waves have been actually observed and identified, as predicted by the theory: in the Kanto and Osaka plains in Japan (Seo and Kobayashi, 1980; Yamanaka *et al.*, 1992; Kagawa *et al.*, 1992; Kinoshita *et al.*, 1992; Yamazaki *et al.*, 1992), in the San Fernando and Los Angeles basins (Liu and Heaton, 1984; Vidale and Helmberger, 1988), and in the Santa Clara valley, California (Frankel *et al.*, 1991). Although all these observations were performed in the low-frequency domain only ($f < 0.5$ to 1 Hz) for large size basins, they may reasonably be thought to be present also in smaller size structures at higher frequencies, and in particular for the discontinuities we address in this paper.

Nevertheless, even when taking 2D diffraction effects and associated surface waves into account, it seems impossible, as already outlined by Yuan *et al.* (1992) for the Shidian basin, to explain the concentration of damages on narrow stripes just in terms of increased amplification of the translational motion: the 30% maximum overamplification with respect to 1D models would only explain an intensity increment of about 0.5°, according to the (fuzzy) published relationships between amplification and intensity (Trifunac and Brady, 1975; Borcherdt and Gibbs, 1976). Meanwhile, actual observations reported in the introduction mention local intensity increments of at least 1°, and in some cases of 2°. As a consequence, as differential motion is the only parameter that is sharply peaked in the vicinity of the discontinuity, we propose that at least part of the damages are related with differential motion.

It is obvious, without the present study, that it is unwise to build structures that span *across* faults or other strong lateral discontinuities. The consistent damage observations reported in the introduction and our numerical results have, in our opinion, two major engineering implications. First, it would not be wise to build structures on soft sites very close to a strong lateral discontinuity, even if this discontinuity does not correspond to an active fault. Second, differential motion might be an important factor in ground motion destructiveness: it is the only ground motion parameter that exhibits a sharp peak near the discontinuity, alike damages, and unlike peak amplitude or spectral amplification. We think that differential motion should receive more attention than presently, and our results stress the need for the installation of new dedicated dense arrays in adequate locations.

REFERENCES

Aki, K. (1988). Local site effects on strong ground motion, in *Earthquake Engineering and Soil Dynamics II: Recent Advances in Ground Motion Evaluation*, J. L. Von Thun (Editor), Geotechnical Special Publication No. 20, Am. Soc. Civil Engr., New York, 103–155.

Aki, K. and K. L. Larner (1970). Surface motion of a layered medium having an irregular interface due to incident plane SH waves, *J. Geophys. Res.* **75**, 933–954.

Bard, P.-Y. and M. Bouchon (1985). The two-dimensional resonance of sediment-filled valleys, *Bull. Seism. Soc. Am.* **75**, 519–541.

Bard, P.-Y. and J.-C. Gariel (1986). The seismic response of two-dimensional sedimentary deposits with large vertical velocity gradients, *Bull. Seism. Soc. Am.* **76**, 343–366.

Ben-Zion, Y. and K. Aki (1990). Seismic radiation from a *SH* line source in a laterally heterogeneous planar fault zone, *Bull. Seism. Soc. Am.* **80**, 971–994.

Boore, D. M., K. L. Larner, and K. Aki (1971). Comparison of two independent methods for the solution of wave scattering problems: response of a sedimentary basin to vertically incident SH waves, *J. Geophys. Res.* **76**, 558–569.

Borcherdt, R. J. and J. F. Gibbs (1976). Effects of local geological conditions in the San Francisco Bay region on ground motions and the intensities of the 1906 earthquake, *Bull. Seism. Soc. Am.* **66**, 467–500.

Cavallin, A., T. Crespellani, D. Schiavone, and L. Siro (1986). Indagini sul tereno, Chapter IV of *"Elementi per una guida alle indagini di microzonazione sismica,"* Progetto Finalizzato "Geodinamica," Monografie finali, CNR, Roma, **Vol. 7** (in Italian).

Chiocchini, U. and C. Cherubini (1986). Seismic microzoning of the Lioni village destroyed by the November 23rd, 1980 earthquake (Irpinia, Campanio-Lucano, Appenine), in *Proc. Int. Symp. Eng. Geology Problems in Seismic Areas*, Vol. 3, Bari, 13–19 April 1986, 341–362.

Day, S. M. and J. B. Minister (1984). Numerical simulation of attenuated wavefields using a Padé approximant method, *Geophys. J. R. Astr. Soc.* **78**, 105–118.

Dezfulian, H. and H. B. Seed (1969). Seismic response of soil deposits underlain by sloping rock boundaries, *Rep. EERC 69-9, UC Berkeley.*

Dezfulian, H. and H. B. Seed (1969). Response of non-uniform soil deposits to travelling seismic waves, *Report EERC 69-13, UC Berkeley.*

Emmerich, H. and M. Korn (1987). Incorporation of attenuation into time-domain computations of seismic wave fields, *Geophysics* **52**, 1252–1264.

Faccioli, E. (1991). Seismic amplification in the presence of geological and topographic irregularities, in *Proc. 2nd Int. Conf. Recent Adv. Geotechnical Earthquake Eng. Soil Dyn.*, Vol. 2, 11-15 March, St. Louis, Missouri, 1779–1797.

Frankel, A., S. Hough, P. Friberg, and R. Busby (1991). Observations of Loma Prieta aftershocks from a dense array in Sunnyvale, California, *Bull. Seism. Soc. Am.* **81**, 1900–1922.

Futtermann, W. I. (1962). Dispersive body waves, *J. Geophys. Res.* **67**, 5279–5291.

Ivanovic, S. (1986). The influence of engineering geological conditions on the degree of building damage in the earthquake of April 15, 1979, of the Montenegrin sea coast, in *Proc. Int. Symp. Eng. Geology Problems in Seismic Areas*, Vol. 2, Bari, 13-19 April, 353–363.

Kagawa, T., S. Sawada, and Y. Iwasaki (1992). On the relationship between dependency of earthquake ground motion and deep basin structure beneath the Osaka plain, *J. Physics Earth* **40-1**, 73–83.

Kinoshita, S., H. Fujiwara, T. Mikoshiba, and T. Hoshino (1992). Secondary Love waves observed by a strong-motion array in the Tokyo lowlands, Japan, *J. Physics Earth* **40-1**, 99–116.

Levret, A., C. Loup, and X. Goula (1986). Le séisme de Provence du 11 juin 1909: dépouillement du dossier inédit du Commandant Spiess; interprétation des observations macrosismiques, *Rapport IPSN / DAS / SASC 284,* (in French).

Liu, H. L. and T. H. Heaton (1984). Array analysis of the ground velocities and accelerations from the 1971 San Fernando California earthquake, *Bull. Seism. Soc. Am.* **74**, 1951–1968.

Moczo, P. (1989). Finite-difference technique for SH waves in 2-D media using irregular grids: application to the seismic response problem, *Geophys. J. Int.* **99**, 321–329.

Nasu, M. (1991). Earthquake damage done at right angle to epicentral direction, in *Proc. 2nd Int. Conf. Recent Adv. Geotechnical Earthquake Eng. Soil Dyn.*, Vol. 2, 11-15 March, St. Louis, Missouri, 1339–1346.

Payany, M. (1983). Etude détaillée des dommages en 1909, in "Simulation du séisme provencal de 1909", Dossier technique C, LCPC Paris/CETE Méditerranée, Rapport d'Etude pour la Délégation aux Risques Majeurs (in French).

Poceski, A. (1969). The ground effects of the Skopje July 26, 1963 earthquake, *Bull. Seism. Soc. Am.* **59**, 1–22.

Prescott, W. H. (1982). Circumstances surrounding the preparation and suppression of a report on the 1868 California earthquake, *Bull. Seism. Soc. Am.* **72**, 2389–2393.

Rodriguez, J. L., J. Ramos, and G. Macedo (1988). Respuesta sismica de un estrato limitado por una pared vertical, *Sismodinámica.* **1**, 119–127 (in Spanish).

Sánchez-Sesma, F. J. (1987). Site effects on strong ground motion, *Soil Dyn. Earthquake Eng.* **6**, 124–132.

Seo, K. and H. Kobayashi (1980). On the rather long-period earthquake ground motions due to deep ground structures of Tokyo area, in *Proc. 7th World Conf. Earthquake Eng.*, vol. 1, Istanbul, 9–16.

Siro, L. (1983). Breve casistica commentata ed alcune conclusioni più general, in *Indagini di Microzonazione sismica* (Intervento in 39 centri abitati della Campania e Basilicata colpiti dal terremoto del 23 Novembre 1980), Progetto Finalizzato "Geodinamica," Monografie finali, CNR, Roma, pub. **492** (in Italian).

Trifunac, M. D. and A. G. Brady (1975). On the correlation of seismic intensity scales with the peaks of recorded strong ground motion, *Bull. Seism. Soc. Am.* **65**, 139–162.

Vidale, J. E. and D. V. Helmberger (1988). Elastic finite-difference modeling of the 1971 San Fernando, California, earthquake, *Bull. Seism. Soc. Am.* **78**, 122–141.

Weischet, W. (1963). The distribution of the damage caused by the earthquake in Valdivia in relation to the form of the terrane, *Bull. Seism. Soc. Am.* **53**, 1259–1262.

Yamanaka, H., K. Seo, and T. Samano (1992). Analysis and numerical modeling of surface wave propagation in a sedimentary basin, *J. Physics Earth* **40-1**, 57–71.

Yamazaki, K., M. Minamishima, and K. Kudo (1992). Propagation characteristics of intermediate-period (1-10 seconds) surface waves in the Kanto plain, Japan, *J. Physics Earth* **40-1**, 117–136.

Yuan, Y., B. Yang, and S. Huang (1992). Damage distribution and estimation of ground motion in Shidian (China) basin, in *Proc. Int. Symp. Effects of Surface Geology on Seismic Motion*, Vol. 1, 25-27 March, Odawara, Japan, 281–286.

Zahradník, J., J. Jech, and P. Moczo (1990a). Approximate absorption correction for complete SH seismograms, *Studia Geoph. et Geod.* **34**, 185–196.

Zahradník, J., J. Jech, and P. Moczo (1990b). Absorption correction for computations of a seismic ground response, *Bull. Seism. Soc. Am.* **80**, 1382–1387.

APPENDIX A

Let us cover a rectangular computational region by an irregular grid with grid spacing $_x h_i$ and $_z h_l$ in the horizontal and vertical directions, respectively:

$$_x h_i = x_i - x_{i-1}, i = 2, \ldots, MX, x_1 = 0, _x h_1 = 0,$$
$$_z h_l = z_l - z_{l-1}, l = 2, \ldots, MZ, z_1 = 0, _z h_1 = 0.$$

Let us denote

$$_x \hbar_i = (_x h_i + _x h_{i+1})/2, \, _z \hbar_l = (_z h_l + _z h_{l+1})/2,$$

where Δt = time spacing, $t_k = (k - 1)\Delta t$, $U_{i,l}^k$ = discrete approximation of the displacement $u(x_i, z_l, t_k)$, and $\xi_{j,i,l}$ = discrete approximation of the function $\xi_j(x_i, z_l, t_k)$ at a grid point i, l at kth time level.

The effective shear moduli $\mu_{i,l}^H$ and $\mu_{i,l}^V$ measure changes of the shear modulus between grid points and are defined as follows:

$$\mu_{i,l}^H = {}_x h_{i+1} \left(\int_{x_i}^{x_{i+1}} dx / M_U(x, z_l) \right)^{-1},$$

$$\mu_{i,l}^V = {}_z h_{l+1} \left(\int_{z_l}^{z_{l+1}} dz / M_U(x_i, z) \right)^{-1}. \tag{A1}$$

The discrete approximation of the density $\rho_{i,l}$ in the grid point i, l is determined as follows:

$$\rho_{i,l} = (\rho_{i,l}^{LR} + \rho_{i,l}^{UD})/2, \tag{A2}$$

$$\rho_{i,l}^{LR} = (1/_x \hbar_i) \int_{x_i - ({}_x h_i/2)}^{x_i + ({}_x h_{i+1}/2)} \rho(x, z_l) dx,$$

$$\rho_{i,l}^{UD} = (1/_z \hbar_l) \int_{z_l - ({}_z h_l/2)}^{z_l + ({}_z h_{l+1}/2)} \rho(x_i, z) dz.$$

Let us introduce new quantities $P_{j,i,l}^H$ and $P_{j,i,l}^V$ in the following way (see equations 7 and 8 and compare with equations 6 and A1):

$$P_{j,i,l}^H = {}_x h_{i+1} \left(\int_{x_i}^{x_{i+1}} dx / \left(M_U(x, z_l) Y_j(x, z_l) \right) \right)^{-1},$$

$$P_{j,i,l}^V = {}_z h_{l+1} \left(\int_{z_l}^{z_{l+1}} dz / \left(M_U(x_i, z) Y_j(x_i, z) \right) \right)^{-1}. \tag{A3}$$

Then the following finite-difference schemes for equations (6) and (7) can be found:

$$U_{i,l}^{k+1} = 2U_{i,l}^k - U_{i,l}^{k-1} + (\Delta t)^2$$

$$\cdot \left[\left(\mu_{i,l}^H (U_{i+1,l}^k - U_{i,l}^k)/_x h_{i+1} \right. \right.$$

$$- \mu_{i-1,l}^H (U_{i,l}^k - U_{i-1,l}^k)/_x h_i)/_x \hbar_i$$

$$+ \left(\mu_{i,l}^V (U_{i,l+1}^k - U_{i,l}^k)/_z h_{l+1} \right.$$

$$- \mu_{i,l-1}^V (U_{i,l}^k - U_{i,l-1}^k)/_z h_l)/_z \hbar_l$$

$$\left. - \sum_{j=1}^n \left(\xi_{j,i,l}^{k+1/2} + \xi_{j,i,l}^{k-1/2} \right)/2 \right] \bigg/ \rho_{i,l}, \tag{A4}$$

$$\xi_{j,i,l}^{k+1/2} = \xi_{j,i,l}^{k-1/2} (2 - \omega_j \Delta t)/(2 + \omega_j \Delta t) + 2\omega_j \Delta t$$

$$\cdot \left[\left(P_{j,i,l}^H (U_{i+1,l}^k - U_{i,l}^k)/_x h_{i+1} \right. \right.$$

$$- P_{j,i-1,l}^H (U_{i,l}^k - U_{i-1,l}^k)/_x h_i)/_x \hbar_i$$

$$+ \left(P_{j,i,l}^V (U_{i,l+1}^k - U_{i,l}^k)/_z h_{l+1} \right.$$

$$-P^{V}_{j,i,l-1}(U^{k}_{i,l} - U^{k}_{i,l-1})/_{z}h_{l})/_{z}\hbar_{l}\Big]\Big/(2 + \omega_{j}\,\Delta t). \qquad \text{(A5)}$$

As regards the boundaries of the computational region, the plane-wave excitation, the conditions for the spatial grid and time spacings, and an evaluation of the effective elastic parameters (equations A1 and A2), see Moczo (1989). Let us only mention here that Emmerich and Korn (1987) showed that the finite-difference schemes in the viscoelastic case do not require smaller time spacing than in the elastic case.

The quantities $P^{H}_{j,i,l}$ and $P^{V}_{j,i,l}$ defined by equations (A3) are evaluated approximately by

$$P^{H}_{j,i,l} = Y^{H}_{j,i,l} \cdot \mu^{H}_{i,l}, \qquad P^{V}_{j,i,l} = Y^{V}_{j,i,l} \cdot \mu^{V}_{i,l},$$

where quantities $Y^{V}_{j,i,l}$ are determined in the following way: let us introduce the quantity $Q^{V}_{k,i,l}$:

$$Q^{V}_{k,i,l} = \left(\int_{z_{l}}^{z_{l+1}} Q_{k}(x_{i}, z)\,dz\right)\Big/ {}_{z}h_{l+1}. \qquad \text{(A6)}$$

$Q^{V}_{k,i,l}$ measures how Q_{k} (the quality factor at the frequency $\hat{\omega}_{k}$) changes along the ith grid column between the grid points i, l and $i, l + 1$. Having K values $Q^{V}_{k,i,l}$ (corresponding to the grid point i, l and to K frequencies $\hat{\omega}_{k}$), we can use the system of equations (4) to determine n quantities $Y^{V}_{j,i,l}$. Assuming $K > n$, the system is solved by a least-squares algorithm.

$Y^{H}_{j,i,l}$ are determined in a similar way.

Finally, we remark that differences between equations (6) and (7), schemes (A4) and (A5), and the definition of ξ_{j} in this paper and the analogous ones in the paper of Emmerich and Korn (1987) are due to a different approach used to construct the finite-difference scheme.

GEOPHYSICAL INSTITUTE   LABORATOIRE DE GÉOPHYSIQUE INTERNE ET TECTONOPHYSIQUE
SLOVAK ACADEMY OF SCIENCES   OBSERVATOIRE DE GRENOBLE
DÙBRAVSKÁ CESTA   UNIVERSITÉ JOSEPH FOURIER
842 28 BRATISLAVA, CZECHOSLOVAKIA   IRIGM, BP 53 X
   (P. M.)   38041 GRENOBLE CEDEX, FRANCE
DEPARTMENT OF PHYSICS   (P.-Y. B.)
UNIVERSITY OF ALBERTA   LABORATOIRE CENTRAL DES PONTS-ET-CHAUSSÉS
EDMONTON, ALBERTA T6G 2J1   58 BD LEFEBVRE
CANADA   75732 PARIS CEDEX 15, FRANCE
   (P. M.)   (P.-Y. B.)